CrossMark

3D structured nanocomposites by FDM process: a novel approach for large-scale photocatalytic applications

Z. Viskadourakis[1] · M. Sevastaki[1,2] · G. Kenanakis[1] (iD)

Abstract

In this work, we report for the first time the fabrication of nanocomposite polystyrene filaments enriched with ZnO and TiO_2 nanoparticles with mass concentrations up to 20%w/w, and the production of 3D photocatalytic structures using a typical FDM-type 3D printer. We provide evidence that the fabricated 3D structures offer promising photocatalytic properties, reaching an efficiency of almost 70% after five cycles of reuse in 20 ppm of Methylene Blue aqueous solution, under UV irradiation. Thus, a novel low-cost alternative route for fabricating large-scale photocatalysts, suitable for practical real-life applications, is proposed.

1 Introduction

Nowadays, a greatly important issue, regarding water pollution, is the remaining contaminants from various organic, highly toxic, persistent pollutant sources, i.e. chemicals, pharmaceuticals, and personal care products. For example, textile industries generate wastewaters that contain considerable amounts of non-fixed dyes, especially of azo-dyes, and a huge amount of inorganic salts. In any case, the reduction (or even better the elimination) of waste water in the ecosystem is of essential significance [1–3]. The most common treatment methods, including adsorption, biological degradation, chlorination or ozonation, are not efficient enough to remove the waste compounds from the treated water streams [4, 5]. Among the new oxidation methods, advanced heterogeneous photocatalysis is a potentially promising technology, since it implies the use of an inert catalyst, non-hazardous oxidants and UV and/or visible light input [6–17].

The ability of semiconductor photocatalysts, such as TiO_2 and ZnO, to degrade a range of organic pollutants, offers many potential applications in areas, such as water and air purification and self-cleaning surfaces [6]. In particular,

TiO_2 has been widely studied and used as photocatalyst [7, 10–13], due to its chemical stability, nontoxicity as well as its low price. However, the photocatalytic efficiency of TiO_2 is limited under visible light due to its wide band-gap (3.0–3.2 eV). On the other hand, ZnO is direct band-gap semiconductor, which has emerged as a considerably promising candidate in the field of photocatalysis [14–18]. Both of them are commercially available as powders; thus their use in waste water treatment requires a separation process, as a post treatment process, to be removed from the water, after photocatalysis [19, 20]. Furthermore, photocatalytic activity increases with effective surface area, and consequently a nanostructured ZnO or TiO_2 is favorable. However, solid structures consisting of nanostructured catalysts, in most cases cannot exceed an overall size of one square inch, due to the limitation of the fabrication techniques, limiting their potential use in practical real-life applications. Thus, the elimination of this last step in the sequence of the waste water purification is highly desirable. Therefore, solid three-dimensional structures, which will include photocatalytic active TiO_2 and/or ZnO phases, would be beneficial, since they will be used as efficient photocatalysts, and then there will not be any requirement of separation of the catalyst from the water [21, 22].

Three-dimensional (3D) printing technology incorporates techniques in which a material is deposited in a layer-by-layer manner, towards the production of three-dimensional objects, of the order of tens of centimeters. Several 3D printing techniques have been developed; however, the most common one is the so-called Fused Deposition Modeling

✉ G. Kenanakis
  gkenanak@iesl.forth.gr

1 Institute of Electronic Structure and Laser, Foundation for Research and Technology-Hellas, N. Plastira 100, 700 13 Heraklion, Crete, Greece

2 Department of Chemistry, University of Crete, 710 03 Heraklion, Crete, Greece

(FDM), in which melted polymeric materials are ejected through a narrow nozzle, to form complicated 3D structures. Materials mostly used in FDM are polymers, such as polystyrene (PS), acrylonitrile butadiene styrene (ABS), polylactic acid (PLA), to name but a few. Long cylindrical cords of the above polymers, known as filaments, are heated above their glass transition temperature, to become soft and flexible, and then they are extruded through a nozzle. This nozzle is movable along all three *xyz* directions and it is computer-controlled. Nozzle movements are determined through computer-assisted design (CAD) files; thus by designing the appropriate structure in a CAD program, nozzle starts to draw the desired pattern, layer by layer, by extruding the molten filament, so that the final structure is built up in such way, on a plain surface.

3D printing technology has already taken much interest in several fields of the research, such as medicine, chemistry and materials science, as an alternative, trendy, effective, fancy, quick and low-cost route for production of 3D samples [23–27]. Therefore, 3D printing emerges as the most efficient technique for the production of (multi)functional materials. Such 3D printing capabilities can be further increased using custom-made filaments rather than commercially available ones. For example, custom-made filaments can be produced by incorporating nanoparticles of inorganic materials into a polymeric matrix, towards the production of a new filament with dedicated properties. Considering that nanoparticles keep their own properties unaffected, after the blending with the polymer matrix, the produced filament could exhibit corresponding functionalities. However, it should be noted that although there are several reports on 3D structures for novel environmental applications [28–30], there are quite a few ones, in which custom-made filaments are used in combination with FDM technology, i.e. in [31]. Thus, it becomes quite interesting to develop filaments enriched with nanoparticles of photocatalytic materials and build 3D structures with potential photocatalytic activity. This way several prototypes and real scale photocatalytic samples can be grown, suitable for real-life applications such as industry exhausts, liquid waste pipelines, etc.

Herein, we report on the production of nanocomposites, consisting of polystyrene PS and commercially available ZnO and/or TiO_2 nanoparticles, in mass concentrations, as high as 20%w/w. These polymer nanocomposites are used to produce custom-made photocatalytic filaments compatible with commercial FDM 3D printers. Then, 3D printed structures have been constructed, and their photocatalytic properties have been studied. Experimental results show that the fabricated 3D printed structures exhibit promising photocatalytic performance, reaching an efficiency of almost 70% after five cycles of reuse in 20 ppm of Methylene Blue aqueous solution, under UV irradiation. To the best of our knowledge, it is the first time that such 3D printed photocatalytic structures are constructed, using home-made filaments, which include photocatalytically active nanofillers.

2 Experimental details

2.1 Synthesis of the metal oxide polymeric nanocomposites

Commercially available PS beads of ~0.5 mm diameter were dissolved in toluene (in sealed bottle, under continuous stirring for 2 h) to create a 20%w/v solution. The resultant solution was stirred for 24 h at room temperature using a magnetic stirrer to yield a homogeneous, milky solution. Appropriate amount of ZnO nanoparticles (mean particle size: 100 nm, obtained from Aldrich) was introduced into 10 ml of the PS/toluene solution, under continuous stirring at 40 °C, so as to obtain a homogeneous suspension, of volume concentration 20%w/v. After 30 min of stirring, 200 ml of ethanol is included and a dense precipitate is formatted. This precipitate is actually a homogeneous nanocomposite, consisting of the PS matrix and the ZnO nanoparticles. After its formation, the nanocomposite is collected and dried at 60 °C for 24 h. Employing such procedure a final mass of 20g of PS/ZnO nanocomposite is produced, the mass concentration of which is 20%w/w. Similar procedure is followed with TiO_2 nanoparticles (mean particle size of ~25 nm, purchased from Evonic Industries) and 20gr of PS/TiO_2 nanocomposite is also produced, with mass concentration of 20%w/w.

2.2 Filament production

The produced PS/metal oxide nanocomposites were cut into small pieces, and they were furtherly dried at 60 °C for 24 h. After that, they were pushed into a home-made filament extruder, which has been pre-heated at 240 °C, and a cylindrical filament with a diameter of 1.75 ± 0.15 mm was produced, which is appropriate for FDM 3D printing. All extrusion parameters, such as temperature and extrusion velocity, have been optimized, towards the production of a uniform continuous cylindrical cord, with an overall length of ~3 m.

2.3 Production of 3D-printed photocatalytic structures

Two different 3D structures were designed (Fig. 1) using "Tinkercad"(free online 3D design and 3D printing software from Autodesk Inc.). The first structure is simple rectangular-shaped (10 mm × 10 mm × 1 mm) samples, while the second is rectangular with cylinders developed in one of the large surfaces. The cylinders were designed to have diameter
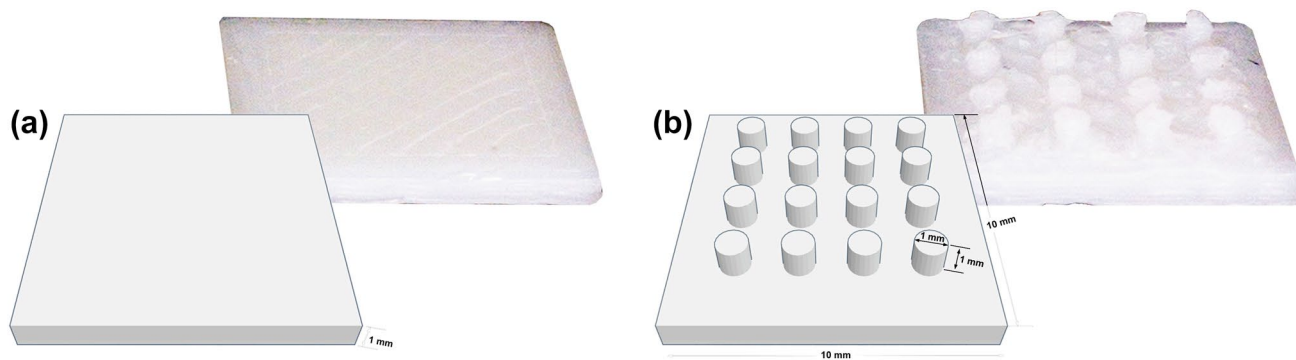
Fig. 1 **a** CAD designs and corresponding optical microscopy photographs **b** of the studied structures. For 3D printed structure in the right (**b**), cylindrical pillars are printed, according to the design; however, they are not perfectly shaped

of 1 mm, height 1 mm, and the distance between neighbor cylinders is 1 mm. All cylinders were placed at the top of the rectangular surface. The purpose of adding the cylinder pillars in the second structure is to increase the area of the structure, and thus to explore whether this will increase the photocatalytic activity of the 3D printed structure.

A dual-extrusion FDM 3D printer (Makerbot Replicator 2X) was used for the direct fabrication of photocatalytic structures, using the homemade filament described above. During printing, nozzle temperature was 240 °C, nozzle speed was 50 mm/s, extrusion speed was 10 mm/s and the bed temperature was 80 °C.

2.4 Characterization and photocatalytic experiments

The crystal structure of the 3D printed samples was determined by X-ray diffraction (XRD) using a Rigaku (RINT 2000) diffractometer with Cu Kα ($\lambda = 1.5406$ Å) X-rays for $2\theta = 20.00$–60.00 for TiO_2 based samples and $2\theta = 30.00$–70.00 for ZnO based samples, respectively, and a step time of 60/s.

Moreover, Raman measurements were performed at room temperature using a Horiba LabRAM HR Evolution confocal micro-spectrometer, in backscattering geometry (180°), equipped with an air-cooled solid-state laser operating at 532 nm with 100 mW output power. The laser beam was focused on the samples using a 10x Olympus microscope objective (numerical aperture of 0.25), providing a ~ 14 mW power on each sample. Raman spectra over the 100–700 cm^{-1} wavenumber range (with an exposure time of 5 s and 3 accumulations) were collected by a Peltier-cooled CCD (1024×256 pixels) detector at -60 °C, with a resolution better than 1 cm^{-1}, achieved thanks to an 1800 grooves/mm grating and an 800 mm focal length. Test measurements carried out using different optical configuration, exposure time, beam power and accumulations to obtain sufficiently informative spectra using a confocal hole of 100 μm, but

ensuring to avoid alteration of the sample, while the high spatial resolution allowed us to carefully verify the sample homogeneity. The Raman shift was calibrated automatically using LabSpec 6 software (Horiba) using zero order line and Si line of a Si reference sample (520.7 cm^{-1}), and the acquired spectra were compared with scientific published data and reference databases, such as Horiba LabSpec 6.

The photocatalytic activity of the 3D printed samples was quantified by means of the decolorization of methylene blue (MB) in aqueous solution, which is a typical potent cationic dye that has been widely used as a model organic to probe the photocatalytic performance of photocatalysts [1, 16, 32–34]. The investigated samples were placed in a custom-made quartz cell, and the whole setup (cell + solution + sample) was illuminated up to 60 min using a UV lamp centered at 365 nm (Philips HPK 125 W) with a light intensity of ~ 6.0 mW/cm^2. The MB concentration (decolorization) was monitored by UV–Vis spectroscopy in absorption mode (absorption at λ_{max}, 665 nm), using a K-MAC SV2100 spectrophotometer over the wavelength range of 220–800 nm. In such way, UV–Vis absorption data were collected at 0 min, 10 min, 20 min, 30 min and 40 min, while the quantification of the MB removal (and hence the remained MB concentration) was estimated by calculation of the area below the main MB peak in the range of 540–700 nm. Additional blank experiments (photolysis) without a catalyst were also performed as well as dye adsorption experiments in the dark.

3 Results and discussion

Figure 1 shows typical optical images from the 3D printed structures, in comparison to the CAD designs. Plain structures were printed with rather smooth surfaces (Fig. 1a), while printing directions are also observed. On the other hand, structures with cylindrical pillars (Fig. 1b) are quite rough, and most of the cylinders seem to be incompletely printed, indicating the low 3D-printing quality of such

structures. In general FDM printing quality is affected by several parameters, such as printing speed, printing temperature, the type of the printer as well as the type of the filament. Especially for the filament, composition, mechanical properties, thermal behavior as well as the process followed for its formation, could possibly affect the quality and the resolution of the final 3D printed object [31, 35–37]. For commercial available filaments, with well-defined compositional, mechanical and thermal properties, all these parameters have been optimized by printer manufacturers, and FDM printers can print samples with resolution as high as 50–100 μm. In our case the filaments used are custommade. Thus the nanoparticle loading (20%w/w) most likely affects the mechanical and thermal properties of the nanocomposite filament and consequently leads to a low resolution/low quality 3D printing. It hence becomes clear that further investigation is needed in order to improve the printing quality; however, as shown later, even with this quality level achieved, the photocatalytic performance of the cylindrical pillar structure is significantly enhanced.

Figure 2 presents typical XRD patterns for both PS/ZnO and PS/TiO$_2$ 3D printed structures. The PS/ZnO samples (Fig. 2a) exhibit sharp diffraction peaks corresponding to wurtzite hexagonal phase, in agreement with the JCPDS card (No. 36-1451). Regarding the PS/TiO$_2$ samples (Fig. 2b), well-distinguished diffraction peaks are observed which correspond to both anatase and rutile phase, in good agreement with the JCPDS card (No. 84-1286) and JCPDS card (No. 88-1175) for a crystal structure of anatase and rutile, respectively [38, 39]. No secondary phases are observed, within the resolution of the instrument.

Figure 3 shows the Raman spectra of both PS/ZnO and PS/TiO$_2$ 3D printed structures. PS/ZnO samples (Fig. 3a) exhibit characteristic ZnO phonon frequencies, in agreement with the literature [9, 40, 41], such as: 334 cm^{-1} (multiple-phonon scattering processes), 376 cm^{-1} (A_1(TO)), 437 cm^{-1} (E_2(high)) and 582 cm^{-1} (E_1(LO)), while the PS Raman peaks can be easily identified [42, 43]. Figure 3b shows a typical Raman spectrum of the PS/TiO$_2$ 3D printed structures, which exhibit characteristic TiO$_2$ phonon frequencies, such as: 145 cm^{-1} (E_g), 398 cm^{-1} (B_{1g}), 518 cm^{-1} (A_{1g}) for anatase, and 244 cm^{-1} (two-phonon scattering) and 612 cm^{-1} (A_{1g}) for rutile, matching (± 2 cm^{-1}) with literature [44–46].

We evaluated the photocatalytic activity of the 3D printed nanocomposites under UV-A light by assessing the decolorization of MB dye in aqueous solution. The photolytic removal of the dye in the absence of any photocatalyst was negligible, underlining the indispensability of the catalysts. The MB solution gradually faded as the photocatalytic process took place, which indicated that the MB concentration decreased obviously. This phenomenon can be ascribed to the destruction of the whole molecular or the chromophore
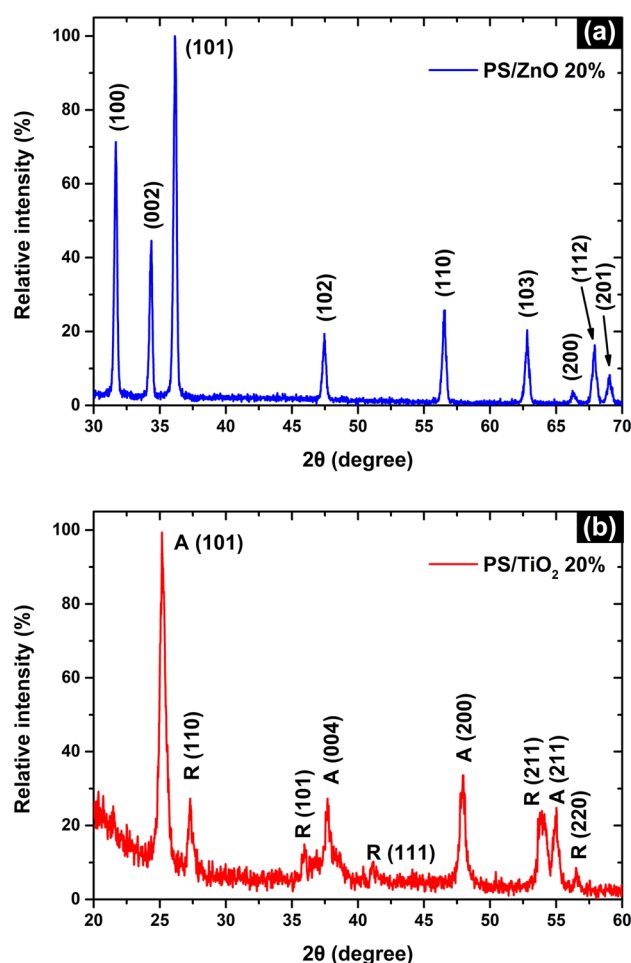

Fig. 2 XRD patterns for both PS/ZnO (**a**) and PS/TiO$_2$ (**b**) 3D printed structures

destruction. Moreover, to eliminate the possibility of dye removal by adsorption on the catalysts, the samples were placed at the bottom of the reactor under dark conditions and in contact with the dye for 30 min, during which time equilibrium of adsorption–desorption was reached. In all cases, removal was insignificant (less than 3%), pointing to the fact that the decolorization of the dye should be attributed to a pure photocatalytic regime.

The decrement of MB concentration (decolorization) for both ZnO and the TiO$_2$ 3D printed nanocomposite samples under UV-A light irradiation is presented in Fig. 4. The photolysis curve (no catalyst present) is also displayed, for direct comparison. According to the photolysis (Fig. 4, black curve), the MB concentration remained almost constant (decreasing from 100% to ~98%) during ~60 min irradiation, indicating that the photolysis of MB was almost negligible.

In addition, the apparent rate constant (*k*) has been calculated as the basic kinetic parameter for the comparison of photocatalytic activities, which was fitted by the equation
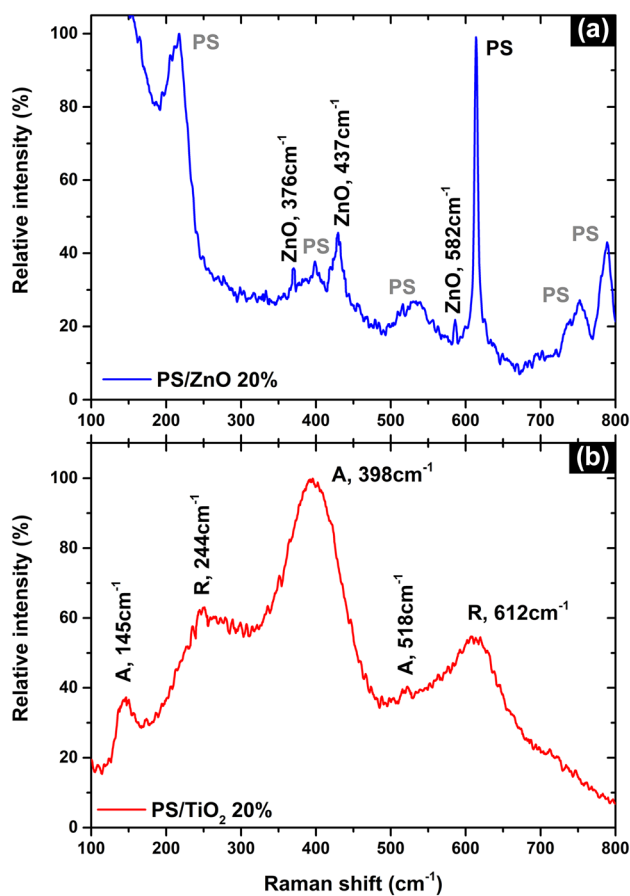
Fig. 3 Raman spectra for both PS/ZnO (**a**) and PS/TiO$_2$ (**b**) 3D printed structures

$\ln(C_t/C_0) = -kt$, where k is apparent rate constant, C_t is the concentration of MB, and C_0 is the initial concentration of MB. It should be noted that the adjusted R-square statistic varies from 0.99738 to 0.99934 indicating that the model used for the determination of the apparent rate constant (k) is satisfactory. The good linear fit of equation $\ln(C_t/C_0) = -kt$ (insets of Fig. 4) confirms that the photodegradation of MB over ZnO and TiO$_2$ photocatalysts follows first-order kinetics. The calculated rate constants were 0.013 and 0.016 min^{-1} for flat and cylinder-based 3D printed ZnO samples, and 0.028 and 0.057 min^{-1} for flat and cylinder-based 3D printed TiO$_2$ samples, respectively. Calculated rate constants are comparable to others previously reported [33, 47]. It is clearly noticed that TiO$_2$ samples are more photocatalytically active than the ZnO ones, regarding the decolorization of MB, reaching an almost 98% MB concentration reduction after 60 min of irradiation. This corroborates the fact that highly oxidative radicals are generated on the TiO$_2$ surfaces, under UV-A irradiation [48], which is not the case with the ZnO.

Moreover, as one can notice from Fig. 4, all the 3D printed samples with the cylinders exhibit much higher photocatalytic activity compared to the flat ones, which can be explained in terms of their larger surface area [14, 30, 33]. In particular, the designed 3D printed TiO$_2$ samples (Fig. 1b) contain 16 cylinders (with Height = Diameter = 1 mm), and thus they should have 2 times larger active area compared to the flat samples (~ 200 mm^2, over 100 mm^2, respectively). Although this is not the case with the corresponding 3D printed samples (cylindrical columns are not perfectly
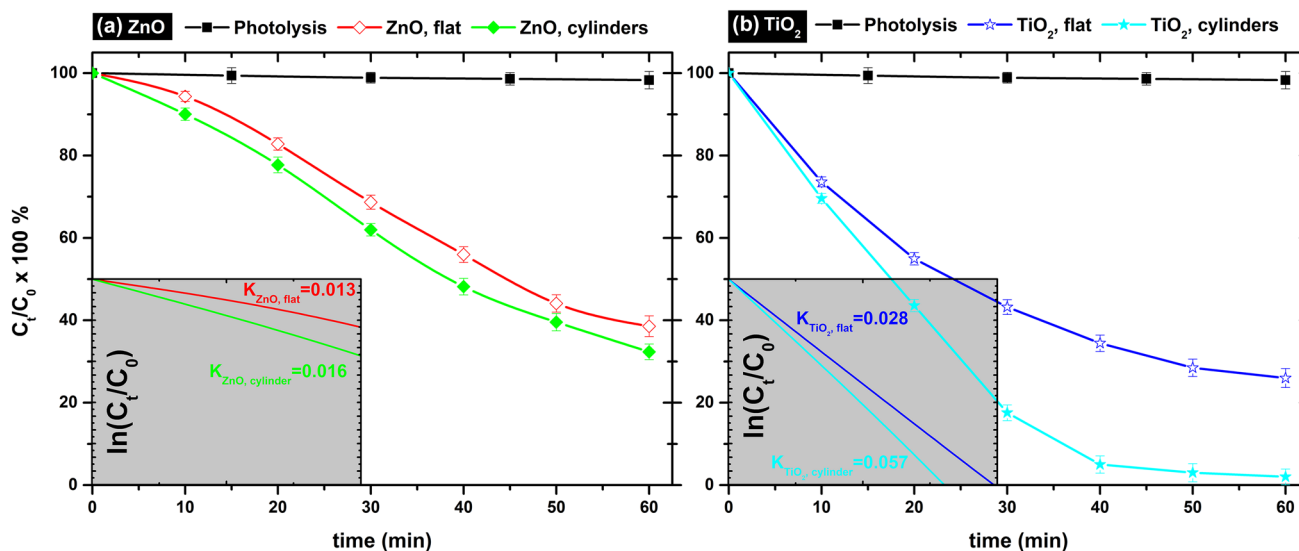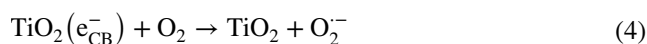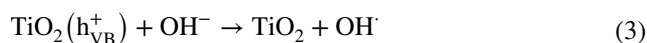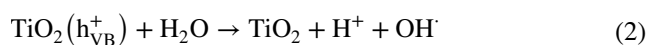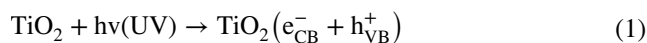

Fig. 4 % MB decolorization over the ZnO (**a**) and the TiO$_2$-based (**b**) 3D printed nanocomposites under UV-A irradiation, vs. irradiation time. Two cases of ZnO and TiO$_2$ nanocomposite samples are presented: flat ones, and samples with 1 mm diameter cylinders [red hollow rhombuses and green solid ones for ZnO in (**a**), and blue hollow rhombuses and cyan solid ones for TiO$_2$ in (**b**), respectively]. In the insets of (**a**) and (**b**) one can see the apparent rate constants (k) for each case. For comparison reasons, the photolysis curve (black solid squares) is also presented

printed), the degradation of the MB, after 60 min irradiation is ~98% for the TiO_2 structure with the cylindrical pillars (~83% in 30 min), compared to ~74% of the flat TiO_2 samples (~67% in 30 min).It should be noted that cylindrical pillar 3D printed samples exhibit smaller surface area than that obtained from the corresponding designed structures. As explained before, this difference is attributed to printing artifacts resulted by the custom-made filaments used. Nevertheless it is still larger than the surface of the flat samples. As a result, the photocatalytic efficiency of the cylindrical pillar structures is improved by 32%, compared to the flat samples, after 60 min irradiation. Finally, it is worth mentioning that the photocatalytic activity tests were carried out for at least five times on our TiO_2 samples to examine their stability under UV illumination, demonstrating negligible changes in the photocatalytic activity after five runs.

In principle, when a semiconductor material is irradiated with a light source of an appropriate wavelength, excitation occurs and electrons (e_{CB}^-) migrate from the valence band to the conduction band of the material, leaving behind positively charged holes (h_{VB}^+). The photogenerated holes will thereafter react with OH^- or H_2O adsorbed on the surface of the catalyst, producing hydroxyl radicals that are mainly responsible for the degradation of the target pollutant. It is, therefore, expected that a high recombination rate of photogenerated holes and electrons will be detrimental for the performance of the photocatalyst.
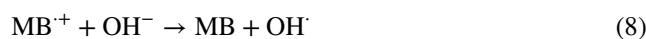
Nevertheless, an efficient electron and hole transfer between TiO_2 and ZnO depends on the difference between the conduction and valence band potentials of the two semiconductors, respectively, that should be suitably positioned [49]. The valence band potential of TiO_2 is more positive than that of ZnO and the conduction band of ZnO is more negative than that of TiO_2, thus allowing charge separation and increasing the efficiency of the photocatalytic reaction [50].

In order to understand the photocatalytic activity of ZnO/TiO_2, one should take into account two key factors that affect photocatalytic mechanism: (a) the ZnO/TiO_2 excitation under light irradiation to generate electron–hole pairs, and (b) the produced reactive oxygen species to degrade organic pollutants [51]. For the case of TiO_2 3D printed structures, a proposed mechanism regarding the TiO_2 photoexcitation and the photosensitized oxidation of MB could be the following [52]:

$$TiO_2 + h\nu(UV) \rightarrow TiO_2\left(e_{CB}^- + h_{VB}^+\right) \tag{1}$$

$$TiO_2\left(h_{VB}^+\right) + H_2O \rightarrow TiO_2 + H^+ + OH^{\cdot} \tag{2}$$

$$TiO_2\left(h_{VB}^+\right) + OH^- \rightarrow TiO_2 + OH^{\cdot} \tag{3}$$

$$TiO_2\left(e_{CB}^-\right) + O_2 \rightarrow TiO_2 + O_2^{\cdot-} \tag{4}$$

$$O_2^{\cdot-} + H^+ \rightarrow HO_2^{\cdot} \tag{5}$$

Electrons and holes are generated in the conduction and the valence band of TiO_2 by UV irradiation, respectively, as shown in (1). The positive holes oxidize hydroxide ions (or water molecule) adsorbed on the surface of TiO_2 particles to produce hydroxyl radicals, as presented in (2) and (3). The electrons of conduction band react with the oxygen to produce superoxide radical anions (4), while the superoxide radical anion reacts with a proton to form hydroperoxyl radicals (5).

For the mechanism of photosensitized oxidation of MB [52], in the presence of catalysts the excited state of MB injects an electron into the conduction band (6). The MB dye is converted to a cationic dye radical that undergoes degradation to yield products according to (7)–(10). The hydroxyl radical existing on the surface of diatomite accelerated the degradation of MB (8):

$$MB^* + TiO_2 \rightarrow MB^{\cdot+}e_{CB}^-\left(TiO_2\right) \tag{6}$$

$$O_2 + e^- \rightarrow O_2^{\cdot-} \tag{7}$$

$$MB^{\cdot+} + OH^- \rightarrow MB + OH^{\cdot} \tag{8}$$

$$MB^{\cdot+} + OH^{\cdot} \rightarrow products \tag{9}$$

$$MB^{\cdot+} + O_2^{\cdot-} \rightarrow products \tag{10}$$

In order to verify the use of our 3D printed nanocomposite photocatalysts for practical environmental applications, we have recovered each sample and tested their efficiency for at least 3–5 runs. Figure 5 depicts the re-use of the 20%w/w cylinder-based TiO_2/PS nanocomposites for five runs. It
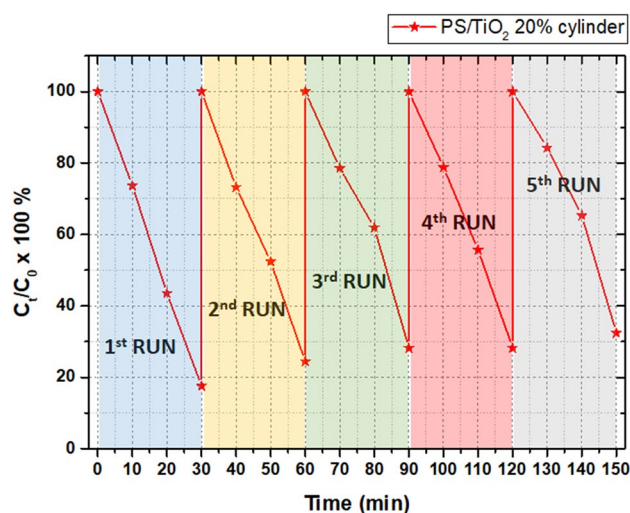

Fig. 5 % MB decolorization over the cylinder-based 20%w/w PS/TiO_2 3D printed nanocomposites under UV-A irradiation, for 5 runs of 30 min irradiation each

is evidently shown that the TiO_2-based 3D printed nanocomposites can be successfully used for at least 5 times for the photodegradation (decolorization) of MB, reaching an efficiency of ~ 72% at the end of the 5th run. Similar stability/reusability tests have been performed to ZnO-based 3D printed samples (not shown here) for 5 runs of 30 min irradiation each. As seen in Fig. 4a, when ZnO-based 3D printed samples were used for the first time, ~ 33% MB could be degraded in 30 min of irradiation (~ 42% degradation of MB, for cylindrical pillar structures). After recovering the ZnO-based samples, and reusing them for a second cycle of 30 min irradiation, the ZnO samples containing cylinders provided a MB decolorization of ~ 37%, while after 5 reusability cycles the MB decolorization decreases to ~ 29%. The reduced photocatalytic efficiency of all the ZnO-based 3D printed samples, compared to the TiO_2 ones, along with their decrease after 5 cycles of reusability could be related to the photocorrosion effect [53, 54].

In order to exploit the photocatalytic properties of the 3D printed samples in practical applications, their mechanical properties should be such that they can be easily incorporated in real devices. In general, a complete analysis of the mechanical properties of any 3D printed sample should involve all the 3D printer bed orientations (flat, on-edge, and up-right), and the raster orientations ($[+45°/-45°]$ $[+30°/-60°]$, $[+15°/-75°]$, and $[0°/90°]$) for the tensile strength test samples [55]. To the best of our knowledge, there is not any report showing that photocatalytic properties are affected by neither the printing orientations nor the mechanical properties. To this point of view such thorough investigation of the mechanical properties is out of the main scope of the manuscript. Nonetheless, preliminary experimental evidence (not shown here) of the mechanical performance of the 3D printed samples was evaluated by means of tensile testing, using a miniature material tester, according to ASTM 638/95 Type V international standard [27], indicating that as the loading concentration (either ZnO or TiO_2) of the polymeric nanocomposites increases, samples become more fragile.

4 Summary and conclusions

Polymeric nanocomposites, consisting of polystyrene matrix and nanoparticles of ZnO and TiO_2 have been produced. Nanoparticle mass concentration of those nanocomposites was 20%w/w. These nanocomposites were then used to form filaments compatible with FDM 3D-printers. Two different 3D-printed structures were constructed using the produced filaments, one flat and another with almost cylindrical pillars on it, and their photocatalytic performance was studied. Up to date, this is the first report on the 3D printing of photocatalytic structures, using custom-made nanocomposite filaments. It is evidently shown that the transition from flat to 3D architectures results in a significant increase of the photocatalytic ability of the samples, due to their increased active surface area reaching an efficiency of ~ 98% after 60 min of UV irradiation (even ~ 83% in only 30 min). The 3D printed nanocomposite samples provide promising photocatalytic properties, reaching an efficiency of almost 70% after five cycles of reuse in 20 ppm of Methylene Blue aqueous solution, under UV irradiation, offering a novel low-cost alternative way for fabricating large-scale photocatalysts, suitable for practical applications.

References

1. C.H. Kwon, H. Shin, J.H. Kim, W.S. Choi, K.H. Yoon, Mater. Chem. Phys. **86**, 78 (2004)
2. I.M. Arabatzis, S. Antonaraki, T. Stergiopoulos, A. Hiskia, E. Papaconstantinou, M.C. Bernard, P. Falaras, J. Photochem. Photobiol. A Chem. **149**, 237 (2002)
3. R.M. Alberici, W.F. Jardim, Appl. Catal. B Environ. **14**, 55 (1997)
4. S.S. Patil, V.M. Shinde, Environ. Sci. Technol. **22**, 1160 (1988)
5. A.T. Moore, A. Vira, S. Fogel, Environ. Sci. Technol. **23**, 403 (1989)
6. A. Mills, S.-K. Lee, J. Photochem. Photobiol. A Chem. **152**, 233 (2002)
7. N. Bahadur, K. Jain, A.K. Srivastava, R. Govind, D. Gakhar, Haranath, M.S. Dulat, Mater. Chem. Phys. **124**, 600 (2010)
8. G. Kenanakis, N. Katsarakis, Appl. Catal. A Gen. **378**, 227 (2010)
9. G. Kenanakis, D. Vernardou, N. Katsarakis, Appl. Catal. A Gen. **411–412**, 7 (2012)
10. K. Soutsas, V. Karayannis, I. Poulios, A. Riga, K. Ntampegliotis, X. Spiliotis, G. Papapolymerou, Desalination **250**, 345 (2010)
11. Y.-H. Peng, G.-F. Huang, W.-Q. Huang, Adv. Powder Technol. **23**, 8 (2012)
12. K. Hashimoto, H. Irie, A. Fujishima, J. Japanese, Appl. Phys. Part 1-Regular Pap. Br. Commun. Rev. Pap. **44**, 8269 (2005)
13. O. Carp, C.L. Huisman, A. Reller, Prog. Solid State Chem. **32**, 33 (2004)
14. G. Kenanakis, Z. Giannakoudakis, D. Vernardou, C. Savvakis, N. Katsarakis, Catal. Today **151**, 34 (2010)
15. X. Chen, Z. Wu, D. Liu, Z. Gao, Nanoscale Res. Lett. **12**, 143 (2017)
16. M.A. Frysali, L. Papoutsakis, G. Kenanakis, S.H. Anastasiadis, J. Phys. Chem. C **119**, 25401 (2015)
17. K.S. Yu, J.Y. Shi, Z.L. Zhang, Y.M. Liang, W. Liu, J. Nanomater. **2013**, 372951 (2013)
18. M.A. Johar, R.A. Afzal, A.A. Alazba, U. Manzoor, Adv. Mater. Sci. Eng. **2015**, 934587 (2015)
19. Y. Li, J. Chen, J. Liu, M. Ma, W. Chen, L. Li, J. Environ. Sci. **22**, 1290 (2010)
20. R. van Grieken, J. Marugán, C. Sordo, P. Martínez, C. Pablos, Appl. Catal. B Environ. **93**, 112 (2009)
21. M.A. Henderson, Surf. Sci. Rep. **66**, 185 (2011)
22. L. Lopez, W.A. Daoud, D. Dutta, Surf. Coatings Technol. **205**, 251 (2010)
23. E. Da Veiga Beltrame, J. Tyrwhitt-Drake, I. Roy, R. Shalaby, J. Suckale, D. Pomeranz Krummel, J. Vis. Exp. **121**, 55427 (2017)

24. C.L. Ventola, P T **39**, 704 (2014)
25. J.-Y. Lee, J. An, C.K. Chua, Appl. Mater. Today **7**, 120 (2017)
26. A. Ambrosi, M. Pumera, Chem. Soc. Rev. **45**, 2740 (2016)
27. G. Kenanakis, K.C. Vasilopoulos, Z. Viskadourakis, N.-M. Barkoula, S.H. Anastasiadis, M. Kafesaki, E.N. Economou, C.M. Soukoulis, Appl. Phys. A **122**, 802 (2016)
28. H.U. Lee, S.C. Lee, Y.-C. Lee, B. Son, S.Y. Park, J.W. Lee, Y.-K. Oh, Y. Kim, S. Choi, Y.-S. Lee, J. Lee, Sci. Rep. **4**, 6740 (2014)
29. L. Hernández-Afonso, R. Fernández-González, P. Esparza, M.E. Borges, S. Dí. González, J. Canales-Vázquez, J.C. Ruiz-Morales, J. Chem. **10**, 846–859 (2017)
30. A.N. Giakoumaki, G. Kenanakis, A. Klini, M. Androulidaki, Z. Viskadourakis, M. Farsari, A. Selimis, Sci. Rep. **7**, 2100 (2017)
31. M.R. Skorski, J.M. Esenther, Z. Ahmed, A.E. Miller, M.R. Hartings, Sci. Technol. Adv. Mater. **17**, 89 (2016)
32. L. Rizzo, J. Koch, V. Belgiorno, M.A. Anderson, Desalination **211**, 1 (2007)
33. G. Kenanakis, N. Katsarakis, J. Environ. Chem. Eng. **2**, 1748 (2014)
34. A. Houas, H. Lachheb, M. Ksibi, E. Elaloui, C. Guillard, J.M. Herrmann, Appl. Catal. B Environ. **31**, 145 (2001)
35. I. Anderson, 3D Print. Addit. Manuf. **4**, 110 (2017)
36. S. Hwang, E.I. Reyes, K. sik Moon, R.C. Rumpf, N.S. Kim, J. Electron. Mater. **44**, 771–777 (2015)
37. Z. Weng, J. Wang, T. Senthil, L. Wu, Mater. Des. **102**, 276–283 (2016)
38. A. Sadeghzadeh Attar, M. Sasani Ghamsari, F. Hajiesmaeilbaigi, S. Mirdamadi, K. Katagiri, K. Koumoto, J. Mater. Sci. **43**, 5924 (2008)
39. S. Bakardjieva, J. Šubrt, V. Štengl, M.J. Dianez, M.J. Sayagues, Appl. Catal. B Environ. **58**, 193 (2005)
40. H. Zhang, D. Yang, S. Li, X. Ma, Y. Ji, J. Xu, D. Que, Mater. Lett. **59**, 1696 (2005)
41. Z. Zhaochun, H. Baibiao, Y. Yongqin, C. Deliang, Mater. Sci. Eng. B **86**, 109 (2001)
42. H.J. Sloane, R. Bramston-Cook, Appl. Spectrosc. **27**, 217 (1973)
43. D.B. Menezes, A. Reyer, A. Marletta, M. Musso, Mater. Res. Express **4**, 15303 (2017)
44. M. Lubas, J.J. Jasinski, M. Sitarz, L. Kurpaska, P. Podsiad, J. Jasinski, Spectrochim. Acta Part A Mol. Biomol. Spectrosc. **133**, 867 (2014)
45. S.F. Shaikh, R.S. Mane, B.K. Min, Y.J. Hwang, O. Joo, Sci. Rep. **6**, 20103 (2016)
46. D.V. Shinde, S.A. Patil, K. Cho, D.Y. Ahn, N.K. Shrestha, R.S. Mane, J.K. Lee, S.-H. Han, Adv. Funct. Mater. **25**, 5739 (2015)
47. S.B. Gajbhiye, Int. J. Mod. Eng. Res. **2**, 1204 (2012)
48. K. Sunada, Y. Kikuchi, K. Hashimoto, A. Fujishima, Environ. Sci. Technol. **32**, 726 (1998)
49. S. Rehman, R. Ullah, A.M. Butt, N.D. Gohar, J. Hazard. Mater. **170**, 560 (2009)
50. A.L. Linsebigler, G. Lu, J.T. Yates, Chem. Rev. **95**, 735 (1995)
51. C.H. Wu, J.M. Chern, Ind. Eng. Chem. Res. **45**, 6450 (2006)
52. I.K. Konstantinou, T.A. Albanis, Appl. Catal. B Environ. **49**, 1 (2004)
53. Y.-Q. Cao, J. Chen, H. Zhou, L. Zhu, X. Li, Z.-Y. Cao, D. Wu, A.-D. Li, Nanotechnology **26**, 024002 (2015)
54. J. Ishioka, K. Kogure, K. Ofuji, K. Kawaguchi, M. Jeem, T. Kato, T. Shibayama, S. Watanabe, AIP Adv. **7**, 035220 (2017)
55. J.R.C. Dizon, A.H. Espera, Q. Chen, R.C. Advincula, Addit. Manuf. **20**, 44 (2018)